Bone Reports 21 (2024) 101774

Contents lists available at ScienceDirect

Bone Reports

journal homepage: www.elsevier.com/locate/bonr

Romosozumab rescues impaired bone mass and strength in a murine model of diabetic kidney disease

Rachel Kohler [a], Dyann M. Segvich [a], Olivia Reul [a], Corinne E. Metzger [b], Matthew R. Allen [b,c], Joseph M. Wallace [a,c,*]

[a] Department of Biomedical Engineering, Indiana University Purdue University of Indianapolis, Indianapolis, IN, United States
[b] Department of Anatomy and Cell Biology, Indiana University School of Medicine, Indianapolis, IN, United States
[c] Roudebush Veterans Administration Medical Center, Indianapolis, IN, United States

ARTICLE INFO

Keywords:
Diabetes
Chronic kidney disease
Bone mechanics
Anabolic
Sclerostin inhibitor

ABSTRACT

As international incidence of diabetes and diabetes-driven comorbidities such as chronic kidney disease (CKD) continue to climb, interventions are needed that address the high-risk skeletal fragility of what is a complex disease state. Romosozumab (Romo) is an FDA-approved sclerostin inhibitor that has been shown to increase bone mineral density and decrease fracture rates in osteoporotic patients with mild to severe CKD, but its effect on diabetes-weakened bone is unknown. We aimed to test Romo's performance in a model of combined diabetes and CKD. 6-week old male C57BL/6 mice were randomly divided into control (CON) and disease model (STZ-Ad) groups, using a previously established streptozotocin- and adenine-diet-induced model. After 16 weeks of disease induction, both CON and STZ-Ad groups were subdivided into two treatment groups and given weekly subcutaneous injections of 100 μL vehicle (phosphorus buffered saline, PBS) or 10 mg/kg Romo. Mice were euthanized after 4 weeks of treatment via cardiac exsanguination and cervical dislocation. Hindlimb bones and L4 vertebrae were cleaned of soft tissue, wrapped in PBS-soaked gauze and stored at —20C. Right tibiae, femora, and L4s were scanned via microcomputed tomography; tibiae were then tested to failure in 4-pt bending while L4s were compression tested. Romo treatment significantly increased cortical and trabecular bone mass in both STZ-Ad and CON animals. These morphological improvements created corresponding increases in cortical bending strength and trabecular compression strength, with STZ-Ad treated mice surpassing vehicle CON mice in all trabecular mechanics measures. These results suggest that Romo retains its efficacy at increasing bone mass and strength in diabetic kidney disease.

1. Introduction

Following a global trend of rising diabetes rates, a CDC survey from 2022 estimated that 37 million Americans currently live with diabetes while an additional 96 million are prediabetic (CDC, 2022). Diabetes is a metabolic disorder characterized primarily by insulin signaling dysfunction, ranging from insulin intolerance driving hyperinsulinemia such as in early type 2 diabetes (T2D), to complete loss of endogenous insulin production as seen in type 1 diabetes (T1D) and late-stage T2D. Long-endured metabolic dysregulation leads to progressive organ damage, such that patients with diabetes are at a higher risk for cardiovascular complications (Navaneethan et al., 2021; Jelinek et al., 2017), dyslipidemia (Jelinek et al., 2017), nephropathy (CDC, 2022; Jelinek et al., 2017), and skeletal weakness. While fracture risk is often overlooked in the face of more pressing comorbidities, fracture and fracture-related mortality rates are increased with both T1D and T2D (Vestergaard, 2007; Farr and Khosla, 2016).

The leading causes of increased fracture risk in diabetic patients are poorly understood, complicated by different presentations in T1D and T2D. In T1D, both bone mass and bone mineral density (BMD) are reduced, leading to higher rates of hip and vertebral fracture in adults (Ha et al., 2021; Weber et al., 2015), and earlier peak-fracture age in children (Eckert et al., 2021), which are often attributed to T1D inhibiting skeletal development (Ha et al., 2021). In contrast, patients with T2D show lower bone turnover markers than healthy age-matched peers (Reyes-García et al., 2013), and as a result often have elevated BMD that confusingly correlates with a 38 % greater risk of hip fracture (Vestergaard, 2007; Farr and Khosla, 2016). Fracture-causing cortical

* Corresponding author at: Department of Biomedical Engineering, Indiana University Purdue University of Indianapolis, Indianapolis, IN, United States.
E-mail address: jmwalla@iu.edu (J.M. Wallace).

https://doi.org/10.1016/j.bonr.2024.101774
Received 7 May 2024; Accepted 10 May 2024
Available online 12 May 2024

porosity can sometimes be masked by normal trabecular micro-architecture in 2D imaging (Farr and Khosla, 2016; Leslie et al., 2012), and obese T2D patients often have larger bones due to load-induced bone growth (Moseley, 2012; Al-Hariri, 2016). However, these documented changes alone do not account for the disparity in fracture risk between T1D, T2D, and healthy patients, suggesting that tissue-level quality defects also increase bone fragility.

Diabetic fracture risk can increase 10-fold with the co-development of chronic kidney disease (CKD), a common comorbidity of diabetes. Impaired glucose control in diabetes can lead to periods of hyperglycemia as well as high blood pressure, both of which overtax kidney blood-filtration, leading to cumulative damage which ultimately results in almost 40 % of patients with diabetes developing CKD (CDC, 2022). Renal dysfunction alone leads to imbalances in bone and mineral metabolism known as CKD-mineral and bone disorder, which in turn causes high bone resorption, cortical porosity, and greatly increased fracture rates and fracture-related mortality (Jelinek et al., 2017; Damasiewicz and Nickolas, 2018). Accordingly, when CKD is comorbid with diabetes, there is a high risk for bone health to be severely impacted (Damrath et al., 2021).

Despite the increasing prevalence of combined diabetes and CKD (diabetic kidney disease, DKD), few clinical trials have examined DKD and fracture risk due to the difficulty of characterizing impacts of this complex and multi-faceted disease state. Current best practice is to refer patients to osteoporosis therapies on a case-by-case basis, usually aiming to preserve bone mass with anabolic or anti-resorptive treatments. However, although bisphosphonates are the gold standard for osteoporosis treatment, they are contraindicated in severe CKD as dosing is difficult to do safely when renal clearance is inhibited (Miller et al., 2022). An alternative treatment may be Romosozumab (Romo), a sclerostin inhibitor that both increases bone formation and decreases resorption (Hsu et al., 2022). Clinical trials have consistently shown that monthly doses of Romo outperform bisphosphonates in increasing BMD and decreasing fracture rates in osteoporotic patients with mild to severe CKD (Miller et al., 2022; Hsu et al., 2022; Miyauchi et al., 2022; Suzuki et al., 2022). While Romo is currently FDA-approved for use in high-risk postmenopausal osteoporosis (Hsu et al., 2022), further investigation is needed to determine its efficacy in increasing bone mass in DKD patients. We hypothesized that Romo would improve bone mass and strength in a murine model of DKD.

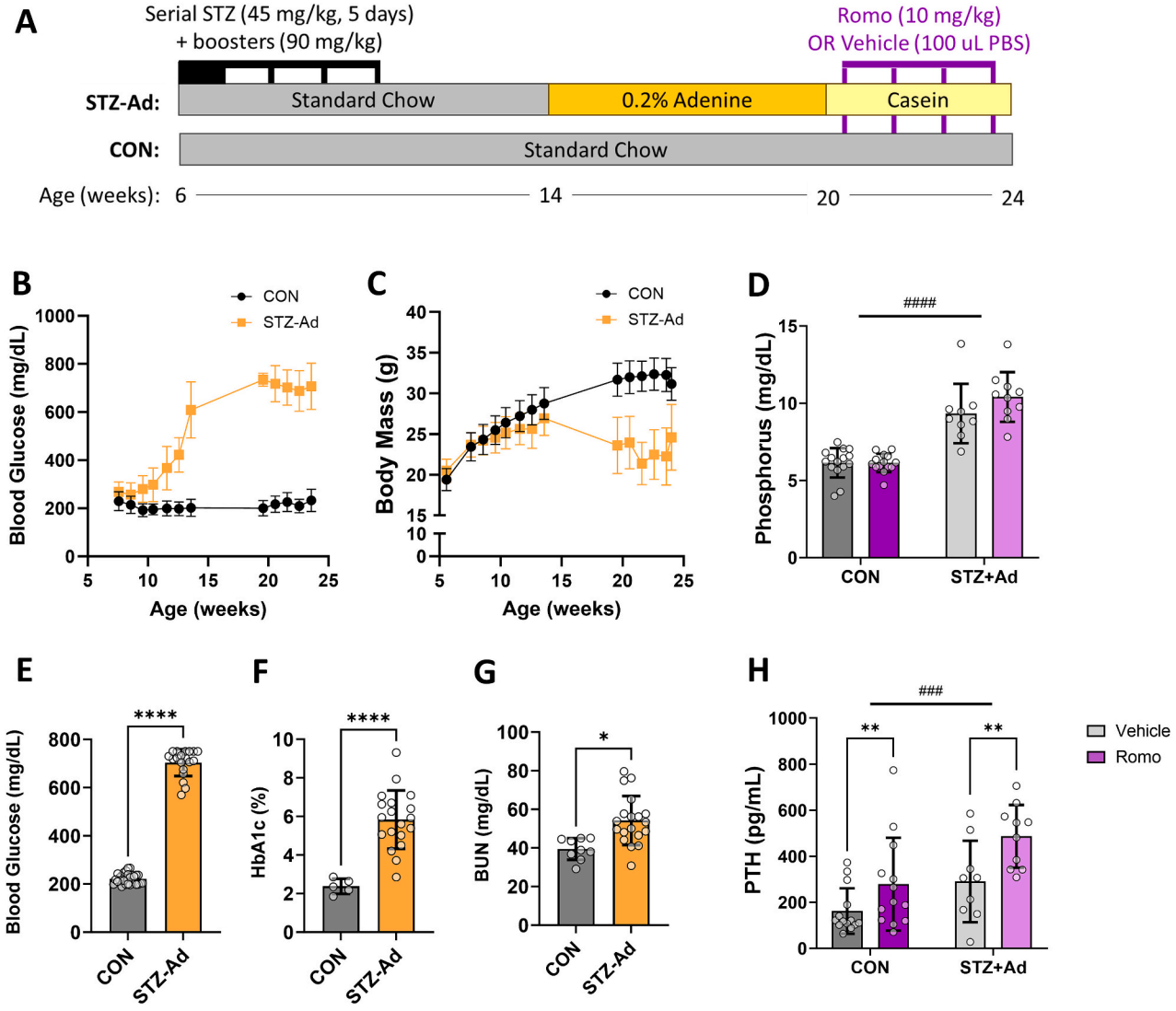

Fig. 1. Disease model characterization. A) Schematic summarizes study timeline, mice were euthanized at 24 weeks of age. STZ-Ad mice developed key features of diabetic nephropathy over the course of the study, with B) development of hyperglycemia C) loss of body weight D) high blood glucose (averaged over last four weeks) that led to E) elevated serum HbA1c. Kidney dysfunction signaling progression of mineral bone disorder was assessed by F) elevated blood urea nitrogen, G) serum phosphorus, and H) serum parathyroid hormone. *P*-values from Student's *t*-test and 2-way ANOVA main effects of disease model (#) and treatment (*) are indicated with e.g. * for $p \leq 0.05$, ** for $p \leq 0.01$, *** for $p \leq 0.001$, and **** for $p < 0.0001$.

2. Methods

2.1. Mouse model

All protocols and procedures were performed with prior approval from the Indiana University School of Medicine Institutional Animal Care and Use Committee. Diabetic nephropathy was induced using a combined model of streptozotocin injections (STZ) and adenine-laced casein diets (Ad). Sixty 6-week old male C57BL/6 mice were randomly divided into disease model (STZ-Ad) and control groups (CON), following previously established models (Fig. 1-A) (Damrath et al., 2022; Hatch et al., 2022). STZ-Ad mice were given 5 daily intraperitoneal injections of streptozotocin (STZ) dissolved no >10 min prior to injection in a 50 mM citrate buffer (45 mg/kg). Metabolic status was monitored for the next 9 weeks, with blood glucose and body weight measures taken weekly to assess development of insulin-deficient hyperglycemia. All instantaneous blood glucose (BG) measures were taken with an AlphaTrak 2 glucometer, using manufacturer-recommended settings for diabetic mice (Zoetis, Parsippany-Troy Hills, NJ, USA). An hour before the first tail nick, mice were given a single dose of 5 mg/kg carprofen (Patterson, Loveland, CO, USA), and just prior to tail nick their tails were dipped in 0.75 % bupivacaine (AuroMedics, East Windsor, NJ, USA) for 30 s. Subsequent blood glucose measures were taken by removing the tail scab. All mice that did not develop blood glucose readings consistently above 300 mg/dL within 2 weeks were given additional single STZ booster shots (90 mg/kg). Glycemia assessments followed by booster dosages were repeated weekly as needed until approximately 2/3 of animals developed hyperglycemia, with some animals receiving up to 3 booster doses. Starting at 14 weeks, STZ-Ad mice were moved to a purified casein diet with altered mineral ratio (0.9 % phosphorous, 0.6 % calcium; Teklad Diets [TD.150303]; Inotiv, Madison, WI, USA) which, for the first 6 weeks, also contained 0.2 % adenine (Ad; Teklad Diets [TD.170948]; Inotiv) to induce kidney damage and development of mineral bone disorder. CON mice were maintained on standard facility provided grain-based chow for the entirety of the study. After 6 weeks, STZ-Ad mice were switched to casein diet without adenine, and both CON and STZ-Ad groups were randomly subdivided into two treatment groups and given weekly subcutaneous injections of 100 μL vehicle (phosphorus buffered saline, PBS) or 10 mg/kg Romo, resulting in the following treatment groups: CON vehicle (CV), CON Romo (CR), STZ-Ad vehicle (DV), and STZ-Ad Romo (DR). After 4 weeks of treatment, mice were euthanized via cardiac exsanguination and cervical dislocation. Pancreas, kidneys, and hearts were immediately harvested, weighed, and fixed in neutral buffered formalin. Whole vertebral columns were excised and wrapped in saline-soaked gauze, while hindlimb bones were cleaned of soft tissue then wrapped in saline-soaked gauze; all bones were stored at −20 °C. During the experiment, 2 animals developed hydrocephaly before treatment, and 1 STZ-Ad mouse began to deteriorate rapidly during the treatment phase; these 3 were euthanized and removed from the study. After HbA1c serum measures (described in the following section), 9 animals were excluded from all further analysis for not developing consistent hyperglycemia (defined as having serum HbA1c levels above 4 % and 4-week average blood glucose above 350), leaving final group sizes of: 15 for CV, 14 for CR, 9 for DV, and 10 for DR.

2.2. Blood serum assessments

2.2.1. GTT and ITT tests

At end of the STZ-induction phase and prior to administration of the adenine diet, glucose tolerance (GTT) and insulin tolerance tests (ITT) were performed on random subsets of STZ-Ad and CON mice (Virtue and Vidal-Puig, 2021). For both tests, fasting blood glucose and body weight measures for each animal were taken just prior to test start. GTT mice were fasted for 6 h, then injected with 1 g/kg glucose solution. BG measures were taken for each animal at 10, 20, 30, 60, 90, and 120 min post-dose. ITT mice were fasted for 2 h, then given a 0.75 U/kg insulin injection at test start. BG measures were taken at 15, 30, 45, and 60 min post-dose. Insulin and glucose tolerance were measured by comparing the area under the curve of readings over time for each specimen (normalized to fasting BG), as calculated in GraphPad PRISM (10.0.2).

2.2.2. Biochemistries

Whole blood aliquots and serum collected from spun down blood samples were stored at −80 °C (Damrath et al., 2022). HbA1c measures were taken from whole blood using a colorimetric assay (Crystal Chem, Elk Grove Village, IL, USA) to assess long-term glycemic control. All STZ-Ad mice with HbA1c values at or below 4 % were excluded from further analyses. Serum was used to measure blood urea nitrogen (BUN) via a urea colorimetric assay (BioAssay Systems, Hayward, CA, USA) to assess kidney function. Serum phosphorus was also measured using a colorimetric assay (Pointe Scientific, Canton, MI, USA), and serum 1–84 parathyroid hormone (PTH) was measured by ELISA (Immunotopics Quidel, San Diego, CA, USA).

2.3. Microcomputed Tomography (μCT)

Hindlimb bones and the 4th lumber vertebra (L4) were cleaned of soft tissue, wrapped in PBS-soaked gauze, and stored at −20 °C, then later thawed and scanned via microcomputed tomography (μCT) in groups of 4 (Kohler et al., 2021; Bouxsein et al., 2010; Reul et al., 2023). Scans were performed using an isotropic voxel size of 8 μm (Skyscan 1272, Bruker, Billerica, MA, USA), scanned through a 0.5 mm Al filter (V = 60 kV, I = 167 μA) with a 0.7-degree angle increment and two frames averaged. Images were reconstructed (nRecon, Bruker) and rotated for consistent analysis (Data Viewer, Bruker) before calibrating to hydroxyapatite-mimicking phantoms (0.3 and 1.25 g/cm^3 CaHA). One kidney and the heart from each animal was also scanned (with no filter), to detect adenine accumulation and overt vascular calcification, with reconstructed slices analyzed with a custom MATLAB program. For each hindlimb bone scan, a binary threshold was applied using the Otsu method, then all voxels representing bone were counted to measure whole bone volume. Trabecular and cortical bone compartments were then analyzed in separate regions of interest (ROI). A 1 mm trabecular ROI was selected starting from the growth plate of each hindlimb bone, extending distally from the proximal growth plate in tibiae and proximally from the distal growth plate in femora. L4 ROIs consisted of first, the trabecular body isolated from the rest of the vertebrae to determine total bone volume, and second, trabecular bone inside the vertebral body (excluding cortical shell). Cancellous architecture in each ROI was quantified using CT Analyzer (CTAn, Bruker). A 0.1 mm cortical ROI was selected at the central midshaft of each hindlimb bone (i.e. at 50 % of bone length; cortical bone was not assessed in L4s). Cortical ROIs were analyzed with a custom MATLAB (MathWorks, Inc. Natick, MA, USA) program. For this study, we added a cortical porosity analysis to this code which counted all void areas within the cortical shell with a size of 250 or fewer voxels as pores (~ 0.015 mm^2 with our 8 μm voxel size), then calculated a percentage porosity by dividing summed pore area by the filled cortical area. For visualization of cortical properties along the length of the bone in femora and tibiae, a second cortical ROI was selected in the central 2/3 s of each bone (from 20 to 80 % of total bone length). Trabecular bone was removed from these whole-bone ROIs using CTAn, and then cortical properties for each slice along the length of the bone were computed with a separate custom MATLAB program. Slice geometry values were averaged for every 1 % of bone length. Bone compartment visualizations were created with Drishti (Limaye, 2012).

2.4. Mechanical analysis

2.4.1. Tibial 4-pt bending tests

Tibiae were tested to failure in four-point bending (lower span at 9 mm; upper span at 3 mm), with the medial surface in tension (TA

Electroforce 5500, New Castle, DE, USA) (Reul et al., 2023). Prior to testing, bones were removed from freezer and placed in a warm room for 1 h to completely thaw. Bones were loaded at a displacement control rate of 0.025 mm/s while the sample was kept hydrated with PBS. After each test, fracture location was measured with calipers and used to select cortical ROIs of the fracture site from μCT scans, which were analyzed using the methods described above. Fracture-site geometry was used to map load-displacement data into stress-strain data using standard engineering equations to estimate tissue level properties. Yield point was determined using the 0.2 % offset method.

2.4.2. L4 compression tests

Vertebral discs and protruding processes were cut from each L4 prior to CT scanning (Jacobson et al., 2023). Thawed bones were placed between flat platens with the vertebral body upright, and compression tested at a displacement rate of 0.02 mm/s to a maximum displacement of 3 mm (Test Resources 500 Universal Test Machine, Shakopee, MN, USA). Output force-displacement data were analyzed in a custom MATLAB software, where the first peak force was taken to be the ultimate force of trabecular bone in the vertebral body and stiffness was calculated as the initial linear slope.

2.5. Histology and tissue analysis

2.5.1. Beta cell mass analysis

Freshly-harvested pancreata were fixed in neutral-buffered formalin for 48 h and then stored in 70 % ethanol before paraffin embedding and sectioning (Damrath et al., 2022). Slices were taken every 4 um along pancreas, and stained for insulin with rabbit anti-insulin antibody (Cell Signaling Technology, Danver, MA, USA). Bright-field images of stained insulin slides were analyzed in a custom ImageJ macro, where images were binarized with two different thresholds to pixels representing insulin-stained and normal pancreas cells, then measured. The mean insulin-over-pancreas area for all slides per specimen was used to approximate functional beta cell mass percent and multiplied by pancreas mass to calculate insulin-producing beta cell mass.

2.6. Fluorescent AGE analysis

Broken right tibiae from bending tests were processed for AGE fluorescence. Bone pieces were demineralized in 20 % EDTA over 1 week, then rinsed, placed in 6 N HCL, and heated at 110 °C for 24 h. Hydrolyzed samples were spun down in a SpeedVac (Thermo Fisher Scientific, SPD140DDA, Waltham, MA, USA) to remove HCL, then rehydrated with 1 mL of HPLC-grade water and filtered using a Nylon syringe filter with 0.2 μm pore size (Thermo Fisher Scientific, 09–720-000). An aliquot of each sample was spun down again, while the remaining sample was used to measure collagen content with a hydroxyproline assay (Sigma Aldrich, St Louis, MO, USA). 200 uL sulfuric acid was added to each spun-down sample, then plated in duplicate in a 96 well plate and measured for fluorescence with a plate reader, alongside quinine standards. Fluorescence measures were normalized to quinine standards and hydroxyproline estimates of collagen mass according to published methods (Vashishth et al., 2001; Karim and Vashishth, 2012).

2.7. Statistics

Kolmogorov–Smirnov tests were performed on all datasets; measures were found to be normally distributed and thus were assessed using parametric tests. Students *t*-tests were performed on measures anticipated to be impacted by the disease model, to verify development of a disease state in STZ-Ad mice compared to controls (Table 1). For all remaining measures, two-way ANOVA tests were performed to assess the contributions of disease and Romo treatment to bone morphology and mechanics, with Tukey post-hoc tests used for any significant interactions. Significance level was chosen to be $\alpha = 0.05$. All data are reported as mean +/− standard deviation unless otherwise noted. All analyses were performed in GraphPad PRISM (10.0.2).

Table 1
Metabolic measures for control and disease model mice.

Metabolic data	CON	STZ-Ad	T-test
	$n = 29$	$n = 19$	*p*-value
Body weight (g)	31.1 ± 2	24 ± 3.7	**<0.0001**
Pancreas (mg)	330 ± 46	248 ± 47	**<0.0001**
Kidney Ave (mg)	201 ± 17	243 ± 30	**0.0003**
Average BG (mg/dL)	222 ± 22	704 ± 55	**<0.0001**
HbA1c (%)	2.38 ± 0.39	5.83 ± 1.51	**0.0001**
GTT AUC	10 ± 3	28 ± 5	**<0.0001**
ITT AUC	5 ± 2	9 ± 3	**0.0016**
BUN (mg/dL)	39.4 ± 5.6	53.6 ± 16.6	**0.0207**

Entries in bold indicate p-values less than the chosen significance value of 0.05.

3. Results

3.1. Disease model presentation

Serial blood glucose measures (BG), GTT and ITT tests, and HbA1C measures all confirmed that STZ induced loss of glycemic control via development of hypoinsulinemia. Pancreata analyses showed that STZ mice had reduced pancreas and beta cell mass compared to controls (Fig. S1). As a result, STZ mice had significantly elevated blood glucose (BG) compared to controls within 4 weeks, which rose and plateaued to an average above 600 mg/dL (Fig. 1-B). This overt hyperglycemia was sustained through the treatment period. BG measures were not taken throughout most of the adenine diet, as mice are known to dislike the taste of adenine and eat less food, as shown by the sharp weight loss after week 14 (Fig. 1-C). Given how delicate mice can become in this comorbid model (Damrath et al., 2022), we did not want to unnecessarily stress them by taking readings that might not be representative of ordinary metabolic function. Regardless, the difference in hyperglycemic control between STZ and CON groups is highlighted by their average BG over the last four weeks of the study, where STZ-Ad measures more than doubled CON (Fig. 1-E), a trend which was also reflected in HbA1c % (Fig. 1-F). In both GTT and ITT tests, STZ mice had higher AUCs than CON mice, showing reduced glycemic control but not loss of insulin sensitivity (Table 1, Fig. S2).

Mice also developed clear signs of nephropathy leading to presentation of early mineral-bone disorder, with hypertrophic kidneys and elevated blood urea nitrogen (BUN), phosphorus, and PTH. As shown in Table 1, kidneys from STZ-Ad mice were much larger than from CON mice, a difference which is only emphasized by STZ-Ad mice also having significantly lower body mass. Serum BUN, a marker of kidney function, was higher in STZ-Ad animals compared to CON (Fig. 1-G), as was serum phosphorus (Fig. 1-D). Serum PTH was increased both by the disease state and Romo treatment (Fig. 1-H).

3.2. Cortical and trabecular morphology

The STZ-Ad disease model was correlated with lower cortical bone measures, but bone mass was somewhat recovered by Romo treatment. In femora, main effects of the disease model were seen with lower total bone volume (BV), bone area, bone area percent (BA/TA), cortical thickness, maximum and minimum moment of inertia (Imax, Imin), and TMD, as well as higher cortical porosity (Table 2, Fig. S3). However, all these measures were higher with Romo treatment (excluding TMD). Similarly in the tibiae, the diseased mice had lower BA/TA, cortical thickness, and higher cortical porosity, while Romo-treated bones had higher BA/TA and cortical thickness (Table 2, Fig. S4). Interaction effects were seen for total area, total BV, bone area, marrow area, Imax, and Imin. For total area, bone area, and inertia measures, this

Table 2
Cortical and trabecular properties for right femora, right tibiae and L4 vertebrae.

Right femora	CON		STZ-Ad		2-way ANOVA main effects		
	Veh ($n = 15$)	Romo ($n = 14$)	Veh ($n = 8$)	Romo ($n = 10$)	Disease	Treatment	Interaction
Total area (mm^2)	2.1 ± 0.18	2.06 ± 0.29	1.84 ± 0.11	2 ± 0.24	0.0961	0.2263	0.4109
Total BV (mm^3)	0.39 ± 0.03	0.44 ± 0.05	0.27 ± 0.03	0.37 ± 0.06	**<0.0001**	**<0.0001**	0.0632
Marrow area (mm^2)	1.14 ± 0.11	1.02 ± 0.18	1.18 ± 0.13	1.14 ± 0.09	0.0633	0.0554	0.3048
Bone area (mm^2)	0.95 ± 0.09	1.04 ± 0.13	0.66 ± 0.1	0.86 ± 0.17	**<0.0001**	**0.0004**	0.1311
BA/TA (%)	45.5 ± 1.3	50.5 ± 2.1	35.9 ± 5.4	42.5 ± 3.9	**<0.0001**	**<0.0001**	0.4168
Cort.Th (mm)	0.22 ± 0.01	0.24 ± 0.01	0.16 ± 0.03	0.2 ± 0.03	**<0.0001**	**<0.0001**	0.2104
Cort.Por (%)	0.19 ± 0.38	0.38 ± 0.52	0.4 ± 0.45	0.96 ± 0.85	**<0.0001**	**0.0099**	0.1264
Imax (mm^4)	0.36 ± 0.06	0.38 ± 0.1	0.22 ± 0.03	0.31 ± 0.09	**<0.0001**	**0.0359**	0.1099
Imin (mm^4)	0.17 ± 0.03	0.18 ± 0.05	0.11 ± 0.02	0.15 ± 0.04	**0.0009**	**0.0349**	0.2037
TMD (g/cm^3 HA)	1.62 ± 0.02	1.64 ± 0.02	1.61 ± 0.02	1.61 ± 0.02	**0.0018**	0.2099	0.5224
BV/TV (%)	19 ± 4.5	25.9 ± 3.6	9.3 ± 1.4	15.1 ± 4.9	**<0.0001**	**<0.0001**	0.6416
Tb.Th (μm)	56.8 ± 4.6	70.5 ± 5	44.3 ± 4.1	62.3 ± 6.2	**<0.0001**	**<0.0001**	0.1591
Tb.Sp (mm)	0.18 ± 0.02	0.16 ± 0.01	0.26 ± 0.02	0.23 ± 0.04	**<0.0001**	**0.0058**	0.5801
Tb.N (1/mm)	3.31 ± 0.59	3.66 ± 0.31	2.13 ± 0.39	2.38 ± 0.59	**<0.0001**	**0.0462**	0.7328

Right tibiae	CON		STZ-Ad		2-way ANOVA main effects		
	Veh (n = 15)	Romo (n = 14)	Veh ($n = 9$)	Romo (n = 10)	Disease	Treatment	Interaction
Total area (mm^2)		1.25 ± 0.18	1.07 ± 0.14	1.26 ± 0.24	**0.009**	0.0566	**0.007**
Total BV (mm^3)	0.34 ± 0.03	0.37 ± 0.04	0.26 ± 0.06	0.33 ± 0.06	<0.0001	<0.0001	**0.0235**
Marrow Area (mm^2)	0.54 ± 0.05	0.45 ± 0.09	0.56 ± 0.13	0.58 ± 0.1	**0.0007**	0.0699	**0.0213**
Bone area (mm^2)	0.75 ± 0.07	0.8 ± 0.09	0.5 ± 0.15	0.68 ± 0.17	<0.0001	0.0001	**0.0221**
BA/TA (%)	58.1 ± 1.6	64.1 ± 2.4	47.08 ± 6.46	53.99 ± 3.8	**<0.0001**	**<0.0001**	0.6788
Cort.Th (mm)	0.22 ± 0.01	0.25 ± 0.01	0.16 ± 0.03	0.2 ± 0.03	**<0.0001**	**<0.0001**	0.1437
Cort.Por (%)	0.6 ± 0.24	0.68 ± 0.31	1.73 ± 0.42	1.92 ± 0.85	**<0.0001**	0.1999	0.6142
Imax (mm^4)	0.15 ± 0.03	0.14 ± 0.04	0.09 ± 0.05	0.14 ± 0.09	0.0009	0.0133	**0.0034**
Imin (mm^4)	0.09 ± 0.01	0.09 ± 0.02	0.05 ± 0.03	0.08 ± 0.04	<0.0001	0.0058	**0.0487**
TMD (g/cm^3 HA)	1.66 ± 0.02	1.66 ± 0.02	1.63 ± 0.02	1.61 ± 0.02	<0.0001	0.0964	**0.026**
BV/TV (%)	18.8 ± 3.3	26.5 ± 3.3	8.96 ± 6.57	15.68 ± 4.87	**<0.0001**	**<0.0001**	0.6295
Tb.Th (μm)	57.1 ± 3.9	70.8 ± 3.5	45.17 ± 10.77	63.27 ± 7.45	**<0.0001**	**<0.0001**	0.1078
Tb.Sp (mm)	0.18 ± 0.02	0.16 ± 0.01	0.24 ± 0.03	0.22 ± 0.03	**<0.0001**	**0.0005**	0.5688
Tb.N (1/mm)	3.28 ± 0.43	3.74 ± 0.33	1.99 ± 0.68	2.45 ± 0.55	**<0.0001**	**0.0006**	0.9808

L4 vertebrae	CON		STZ-Ad		2-way ANOVA main effects		
	Veh (n = 15)	Romo (n = 14)	Veh (n = 9)	Romo (n = 10)	Disease	Treatment	Interaction
BV/TV (%)	22.2 ± 2.9	33 ± 3.3	16.2 ± 1.9	28.4 ± 4.8	**<0.0001**	**<0.0001**	0.4706
Tb.Th (μm)	47.6 ± 4.1	62.4 ± 3.9	40 ± 3.2	58.2 ± 3.8	**<0.0001**	**<0.0001**	0.1416
Tb.Sp (mm)	0.16 ± 0.01	0.14 ± 0.01	0.18 ± 0.01	0.17 ± 0.02	**<0.0001**	**0.0002**	0.8532
Tb.N (1/mm)	4.65 ± 0.33	5.28 ± 0.28	4.38 ± 0.35	5.06 ± 0.62	**0.045**	**<0.0001**	0.8289

Entries in bold indicate p-values less than the chosen significance value of 0.05.

interaction was driven by DV tibiae being smaller than all other groups, while in bone area, CR group was also larger than DR (Fig. 2). For marrow area, CR had smaller tibial marrow cavities than all other groups. fAGEs prevalence in diabetic cortical bone did not significantly differ from controls (Fig. S5).

The largest impacts to bone mass and morphology were seen in trabecular bone. While all trabecular measures in all bones analyzed were lower in the disease model, trabecular bone mass was much higher in Romo-treated animals (Table 2). Main effects of the disease model were seen with lower bone volume percent (BV/TV) from thinner (Tb.Th) and further spaced trabeculae (Tb.Sp) in all bones (Figs. 2, S6). Trabecular number (Tb.N) was also lower in all bones. Conversely, Romo was correlated with increased trabecular thickness and number, with correspondingly higher BV/TV and lower Tb.Sp. Due to these large differences in bone mass between groups, treatment and model-driven impacts on trabecular TMD in hindlimb bones were obscured due to partial volume effects; only L4 trabecular bone showed a main effect of reduced TMD in STZ-Ad mice independent of bone mass (Fig. S7).

3.3. Bending and compression tests

In 4-pt bending tests of right tibiae, STZ-Ad animals had fragile cortical bone that was strengthened by Romo. All whole-bone mechanical properties (with the exception of displacement to yield), and estimated tissue level properties (with the exception of elastic modulus) were lower in the STZ-Ad group (Table 3, Fig. 3). However, Romo treatment resulted in higher yield force, work to yield, and ultimate stress. An interaction effect was only seen for ultimate force, as all CON group measures were larger than STZ-Ad groups, but DR was significantly higher than DV (Fig. 3).

Similarly in compression tests of L4 vertebrae, trabecular bone strength was lower in the disease model but higher with Romo. Only peak force was significantly lower in STZ-Ad trabecular bone, although stiffness trended lower ($p = 0.085$, Table 3). However, this lower compressive strength was completely reversed with Romo, as peak force, peak displacement, and stiffness were all higher with Romo, with the DR group surpassing CV in all measures (Table 3, Fig. 3). Peak force at fracture was closely correlated with bone volume (Fig. 3-I).

4. Discussion

4.1. Combining STZ with a high-mineral diet creates a hyperglycemic CKD model

Using serial STZ injections and a high-phosphorus adenine diet, we successfully produced an insulin-deficient hyperglycemic mouse model

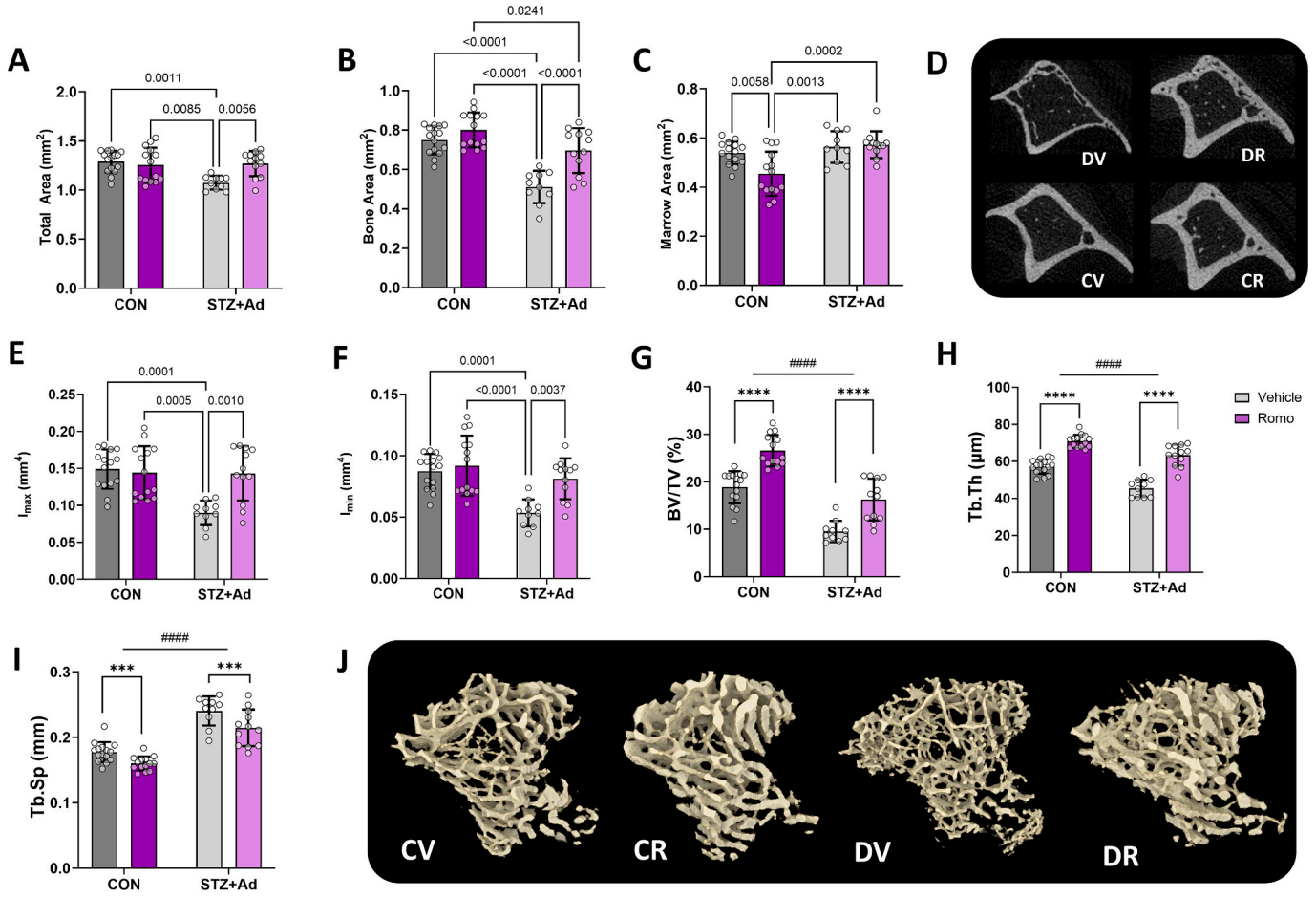

Fig. 2. Tibial geometry measures. Cortical and trabecular bone mass were impacted by both Romo treatment and the disease model. Cortical analysis of μCT scans of right tibiae show that the disease model had reduced cortical midshaft A) total area, B) bone area, C) marrow area, and *E*-F) area moment of inertia, but bone area and overall mass was rescued by Romo treatment, as shown in D) by representative transverse slices from the tibial crest of a bone from each group. Trabecular bone showed large main effects of both Romo and the disease model with changes in G) bone volume percent primarily driven by H) changes in trabecular thickness which I) altered trabecular spacing. J) 3D renders of the proximal trabecular compartment in representative bones from each group. *P*-values from 2-way ANOVAs are shown, with main effects of disease model (#) and treatment (*) indicated with e.g. * for $p \leq 0.05$, ** for $p \leq 0.01$, *** for $p \leq 0.001$, and **** for $p < 0.0001$. Where there was a significant interaction effect *p*-values from Tukey post-hocs are shown numerically. Abbreviations in D and J refer to the treatment groups: CON vehicle (CV), CON Romo (CR), STZ-Ad vehicle (DV), and STZ-Ad Romo (DR).

with impaired kidney function, demonstrating a methodology for modeling this combined disease state. An ongoing limitation of preclinical research in combined diabetes and CKD has been a lack of representative animal models that show both disrupted glucose control and nephropathy. The American Models of Diabetic Complications Consortium (AMDCC), which was created in 2001 by the NIH, established benchmarks by which to measure the efficacy of a given model at representing human diabetic nephropathy (Brosius et al., 2009). Current mouse models often fall short of AMDCC benchmarks in their lack of renal failure, as they are typically extensions of diabetic models attempting to capture incidental nephropathy (AMDCC, 2003). However, as murine glycemic control is notoriously resilient, this resistance may play a role in limiting the downstream effects of high blood sugar on organ damage. Murine resistance to developing diabetes is illustrated in this study, where 1/3 of animals retained sufficient insulin-production to maintain normal blood sugar even after receiving multiple high doses of STZ. Further, while STZ is frequently used to induce hyperglycemia, dosages and accompanying diets vary widely, complicated by the fact that female mice are more resistant to pancreatic damage than males, requiring much higher STZ doses to achieve the same outcome (Hatch et al., 2022; Furman, 2015; Goyal et al., 2016). Here we show that combining STZ with an adenine-laced, high-mineral diet can produce clear hyperglycemic nephropathy in male animals, just as previously shown in females (Damrath et al., 2022).

While elevated BUN and serum PTH indicate kidney dysfunction, these measures were not as elevated in this study as in other adenine-induced models of CKD, nor did this model retain all the same characteristics of those models. Adenine diets typically induce kidney atrophy, due to the development of damage and fibrosis caused by the accumulation of dihydroxyadenine (DHA) crystals that are opaque in CT (Metzger et al., 2021; Metzger et al., 2020). In the current study, the only animals that had small kidneys with visible DHA were excluded from the study for not developing hyperglycemia, while all hyperglycemic animals had hypertrophic kidneys without any measurable DHA residue (Table S1). As STZ-induced organ hypertrophy has been previously reported (Sharma et al., 1996), and STZ is known to cause renal mesangial expansion and matrix thickening in C57BL/6 mice (Qi et al., 2005; Gurley et al., 2006; Deeds et al., 2011), this observation suggests that kidney dysfunction was primarily driven by STZ and sustained hyperglycemia, with the high phosphorus and/or casein component of the diet possibly contributing to the development of kidney disease. STZ may have induced mesangial expansion prior to the initiation of the adenine diet and prevented DHA from accumulating in kidneys and causing further damage. These results are consistent with our previously published model in female mice, where STZ was shown to mildly "protect" against adenine-induced kidney damage (Damrath et al., 2022). In short,

Table 3
Mechanical properties of right tibiae and L4s from 4-pt bending and compression tests.

4-pt bending mechanics	CON		STZ-Ad		Main Effects		
	Veh (n = 15)	Romo (*n* = 13)	Veh (n = 8)	Romo (n = 10)	Disease	Treatment	Interaction
Yield force (N)	20.4 ± 3.6	21 ± 5	12.9 ± 3.2	15.9 ± 3.6	**<0.0001**	**0.0309**	0.0882
Ultimate force (N)	23.6 ± 3.4	25.3 ± 4.4	13.6 ± 3.4	18.4 ± 3.8	**<0.0001**	**0.001**	**0.0377**
Disp. to yield (μm)	218 ± 15	226 ± 22	218 ± 25	215 ± 15	0.0615	0.7859	0.2603
Postyield disp. (μm)	330 ± 239	411 ± 278	153 ± 200	215 ± 139	**0.0299**	0.3129	0.9677
Total disp. (μm)	549 ± 245	638 ± 275	371 ± 198	430 ± 151	**0.0215**	0.304	0.9006
Stiffness (N/mm)	106 ± 20.9	105.4 ± 28.7	67.9 ± 18	84.6 ± 19.6	**0.0015**	0.0598	0.0501
Work to yield (mJ)	2.35 ± 0.43	2.51 ± 0.62	1.53 ± 0.41	1.85 ± 0.42	**<0.0001**	**0.0362**	0.264
Postyield work (mJ)	5.93 ± 3.87	7.48 ± 3.87	2.03 ± 2.74	3.21 ± 1.62	**0.0007**	0.1745	0.9395
Total work (mJ)	8.28 ± 3.81	9.99 ± 3.6	3.55 ± 2.82	5.06 ± 1.77	**<0.0001**	0.0896	0.9289
Yield stress (MPa)	217 ± 20	221 ± 33	199 ± 26	217 ± 24	**0.0414**	0.4276	0.7593
Ultimate stress (MPa)	253 ± 20	270 ± 29	210 ± 31	251 ± 20	**<0.0001**	**0.0084**	0.4865
Strain to yield (mε)	17.8 ± 1.5	18.3 ± 1.9	16.6 ± 2	16.6 ± 1.3	**0.0011**	0.5698	0.6422
Total strain (mε)	44.7 ± 20.3	50.6 ± 19.4	26.3 ± 10	36.9 ± 18	**0.0095**	0.1181	0.591
Modulus (GPa)	13.9 ± 2	13.6 ± 1.4	13.9 ± 2.1	14.1 ± 2.1	0.4675	0.932	0.643
Resilience (MPa)	2.04 ± 0.23	2.16 ± 0.49	1.79 ± 0.36	1.8 ± 0.28	**0.003**	0.553	0.6117
Toughness (MPa)	7.42 ± 3.66	8.84 ± 3.53	3.8 ± 2.31	5.56 ± 2.55	**0.0017**	0.0979	0.7932

L4 compression mechanics	CON		STZ-Ad		Main Effects		
	Veh (n = 14)	Romo (n = 13)	Veh (n = 9)	Romo (n = 10)	Disease	Treatment	Interaction
Peak force (N)	32.5 ± 9.3	60.7 ± 14.8	20.4 ± 19.2	56 ± 17.6	**0.0354**	**<0.0001**	0.3359
Peak disp. (mm)	142 ± 33	193 ± 54	137 ± 66	184 ± 46	0.6015	**0.0004**	0.854
Stiffness (N/mm)	140.4 ± 38.8	219.1 ± 73.3	82 ± 33	218 ± 76	0.0846	**<0.0001**	0.0925

Entries in bold indicate p-values less than the chosen significance value of 0.05.

it may be possible to induce diabetes with kidney disease in C57BL/6 mice with only STZ and a high-phosphorus casein diet (no adenine), although further research is needed.

4.2. Romo's anabolic activity combats mineral-bone disorder in diabetic nephropathy

Romosozumab was highly effective at building bone in STZ-Ad mice, often to a greater extent than in CON mice, suggesting that its actions as both a resorption inhibitor and a formation catalyst are effective in this hyperglycemic kidney disease model. Romo is a humanized monoclonal antibody that binds to osteocyte-secreted sclerostin, thereby preventing it from inhibiting the Wnt pathway, which upregulates osteoblast activity and indirectly suppresses osteoclast resorption (McClung et al., 2014). Several clinical studies have explored the use of Romo to treat postmenopausal high-risk osteoporosis in mild to moderate CKD (but not diabetes). Overall, Romo has been shown to quickly increase bone mineral density (BMD) and decreases fracture risk (Saito et al., 2023; Geusens et al., 2023). We were able to replicate these clinical findings in this murine model of hyperglycemic CKD, with both DR and CR groups showing increased cortical and trabecular bone mass compared to DV and CV groups, respectively. Measures such as cortical bone volume, bone area, cortical thickness and trabecular BV/TV and Tb.Th were lower in the disease model compared to untreated controls, but higher with Romo treatment in both CON and STZ-Ad groups.

Interestingly, STZ-AD mice saw a greater relative increase in bone mass than CON mice with Romo treatment. Cortical thickness increased an average of 40 μm in DR hindlimb bones as compared to DV, while CR cortical thickness only increased an average of 25 μm compared to CV. These results suggest that a longer treatment period could have led the DR group to fully recover cortical bone mass, to match CV bone mass. Similarly in trabecular bone, Tb.Th increased an average of about 18 μm in all bones of DR mice compared to DV, but only about 15 μm in CR compared to CV. However, DR cortical and trabecular bone still had reduced TMD, suggesting that even if the disease model is more responsive to Romo treatment, bone tissue quality is still hampered by the disease state.

Both Romo treatment and the disease model were correlated with elevated PTH, which may have played a role in several key presentations of altered bone remodeling, namely increased cortical porosity in disease mice and trabecular tunneling with Romo treatment. In clinical presentations of CKD, reduced glomerular filtration efficiency can lead to elevated serum phosphorus, which in turn drives increased expression of PTH. Secondary hyperparathyroidism (SHPT) causes abnormal bone remodeling, with accelerated resorption that leads to vascular calcification, cortical porosity, trabecular tunneling (Misof et al., 2019; Rubin et al., 2011; Sikjaer et al., 2012) (Fig. S8), and increased fracture risk (Jelinek et al., 2017; Damasiewicz and Nickolas, 2018). In both CON and STZ-AD mice, Romo treatment also increased expression of PTH (Fig. 1-H), replicating a presentation seen in clinical trials, where Romo has been shown to reduce circulating serum calcium, driving a reciprocal increase in PTH (Sato et al., 2021; Saag et al., 2017). Porosity, while only mildly increased in this model, was not reduced by Romo treatment (Table 2, Figs. 2-D, S3, S4), a morphology that may have been mediated by altered osteocyte behavior. High PTH has been correlated with increased osteocyte lacunar density and area, which have been shown to be precursors to increased cortical porosity (Misof et al., 2019). Rats with CKD and SHPT have been shown to have reduced mineralization around osteocytes (Hasegawa et al., 2023), while elevated PTH in adenine-induced CKD in mice has been correlated with delayed osteocyte apoptosis (Metzger et al., 2020). However, as PTH levels were comparable between CR and DV mice without comparable porosity, interaction of multiple aspects of the disease state likely led to this presentation.

4.3. Romo-treatment improved bone strength

For all treatment groups, bone strength was proportional to bone mass. 4-pt mechanical tests of cortical bone showed increased fragility in diseased mice. MBD-driven resorption likely increased the tibial marrow area and decreased cortical thickness in STZ-Ad bones, which reduced the area moment of inertia and contributed to decreased bending strength. While Romo treatment increased cortical thickness in both groups, it did not significantly reduce marrow area in the tibial midshaft of STZ-Ad mice (Fig. 2-C), which may explain why cortical bending strength was not fully rescued. In addition, many estimated tissue-level

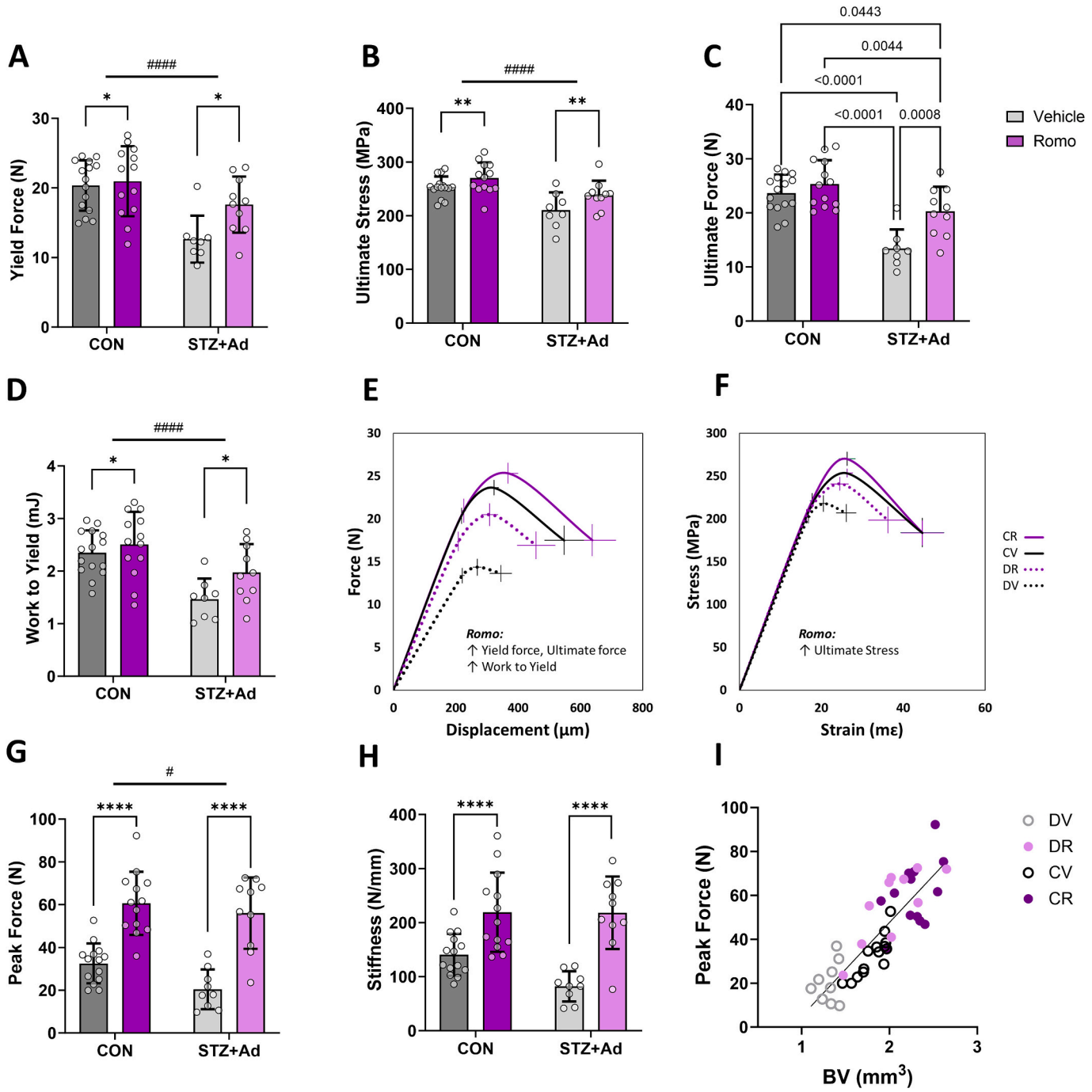

Fig. 3. Mechanical properties from 4-pt bending and compression tests. Plots of A) yield force B) ultimate force, C) ultimate stress and D) work to yield show effects of disease model and Romo treatment on cortical bending strength. Overall trends are shown in summary plots of mechanical tests with (E) mean force and displacement and (F) mean stress and strain values, all plotted at yield, ultimate, and failure points for each group, with error bars showing standard error (SEM). Text inserts summarize significant main effects of Romo from two-way ANOVA. Compression tests of L4a show that Romo increased G) peak force with a corresponding increase in H) stiffness. I) Peak force was correlated with bone volume. *P*-values from 2-way ANOVAs are shown, with main effects of disease model (#) and treatment (*) indicated with e.g. * for $p \leq 0.05$, ** for $p \leq 0.01$, *** for $p \leq 0.001$, and **** for $p < 0.0001$.

properties, such as strain and resilience, were significantly impacted by disease state (with reduced TMD likely playing a role), but not by Romo treatment. Only a single measure, ultimate stress, was increased by Romo treatment, but this could be driven by whole-bone changes, as tissue-level estimates can be skewed by large differences in bone mass in small-scale bending tests. These results provide evidence that metabolic dysregulation caused by hyperglycemia and nephropathy may impact tissue composition in DKD, creating fragility that cannot be fully rescued by anabolic treatment.

In vertebral trabecular bone, the positive impact of Romo on bone mass surpassed the detriment caused by the disease state, resulting in disease model deficits being obscured by the magnitude of compression resistance gained by Romo treatment. While the disease model decreased peak force, Romo treatment rescued it, with DR bone far surpassing the compressive strength of CV bone. The other mechanical measures reported were not significantly impacted by disease, however, this absence may be the product of both the outsized impact of Romo on L4 trabecular bone and limitations of testing small murine L4 bones.

While peak displacement represents the magnitude of deformation at peak force, it is affected by vertebral size and rig-orientation, not just trabecular rigidity. It is worth noting that for trabecular stiffness, there was a trend toward statistical significance for main effects of the disease model and interaction terms due to the stiffness of DV bone being almost half that of CV bone, while DR and CR stiffness are nearly identical. In short, Romo is highly effective at rescuing trabecular bone strength in a DKD model.

4.4. Limitations

This work has several limitations. First, the initial STZ dosage given to male mice (45 mg/kg), was not sufficient to induce hyperglycemia in all animals, requiring booster doses and animal exclusion. Our initial aim was to protect animals from deteriorating too rapidly to ensure they could endure a combination disease state, so we chose a lower dosage that has been used successfully in other published studies (King, 2012). However, as has been repeatedly shown, STZ efficacy varies widely depending on the animal's genetic background and sex (Goyal et al., 2016), and possibly its environmental conditions such as bedding and chow. We are not the first to have used Romo in animal studies (Marino et al., 2023; Sinder et al., 2016), but other studies have used a murine-specific sclerostin antibodies due to concern that the humanized monoclonal anti-sclerostin antibody may encounter some resistance in mice (Li et al., 2009; Ominsky et al., 2017). While we did not have a means of directly measuring antibody action, the substantial impact we saw on bone growth suggests that if there was any resistance in our model, it was at most muted. For the purposes of modeling anti-sclerostin antibody impact on bone growth, we saw no disadvantage to using Romo instead of a mouse-specific analog. The lack of a CON group on the casein diet or an STZ-Ad group on normal chow limited our ability to explain observations that may have been driven by diet. Finally, compression tests of mouse vertebrae are infrequently performed as their small and irregular size makes it difficult to keep bones consistently oriented and properly immobile without the use of custom rigs or removing the processes (as was done here). While μCT scanning of all vertebrae was performed after the processes were removed, it is possible that undetectable small-scale defects were introduced during preparation, impacting bone integrity.

5. Conclusion

This study demonstrates that Romosozumab can quickly rescue bone mass and strength in a murine model of hyperglycemia and altered kidney function analogous to clinical diabetic nephropathy. Romo was especially effective at improving trabecular bone mass, which increased vertebral compression strength. These results suggest that Romosozumab could be used for reducing fracture risk in patients with DKD, especially by reinforcing trabecular bone. Despite Romo's impressive ability to bolster trabecular bone mass and vertebral strength, muted improvement to cortical bending strength point to the continued need to study means of targeting bone quality in diabetic patients.

CRediT authorship contribution statement

Rachel Kohler: Data curation, Formal analysis, Funding acquisition, Investigation, Methodology, Project administration, Software, Visualization, Writing – original draft, Writing – review & editing. **Dyann M. Segvich:** Investigation, Methodology, Project administration, Resources, Supervision, Writing – review & editing. **Olivia Reul:** Investigation, Writing – review & editing. **Corinne E. Metzger:** Investigation, Project administration, Resources, Supervision, Writing – review & editing. **Matthew R. Allen:** Conceptualization, Funding acquisition, Resources, Supervision, Writing – review & editing. **Joseph M. Wallace:** Conceptualization, Funding acquisition, Project administration, Resources, Supervision, Writing – review & editing.

Declaration of competing interest

The authors declare no conflict of interest.

Data availability

Data will be made available on request.

Acknowledgements

This research was funded by the National Institutes of Health and the U.S. Department of Veterans Affairs under grants T32DK064466 and I01 BX005990, respectively. Romosozumab was provided via a material transfer agreement between Dr. Matthew Allen and Amgen.

Appendix A. Supplementary data

Supplementary data to this article can be found online at https://doi.org/10.1016/j.bonr.2024.101774.

References

Al-Hariri, M., 2016. Sweet bones: the pathogenesis of bone alteration in diabetes. J. Diabetes Res. 2016.
AMDCC. Validation of Mouse Models of Diabetic Nephropathy. 2003.
Bouxsein, M.L., Boyd, S.K., Christiansen, B.A., Guldberg, R.E., Jepsen, K.J., Müller, R., 2010. Guidelines for assessment of bone microstructure in rodents using micro–computed tomography. J. Bone Miner. Res. 25 (7), 1468–1486.
Brosius, F.C., Alpers, C.E., Bottinger, E.P., Breyer, M.D., Coffman, T.M., Gurley, S.B., Harris, R.C., Kakoki, M., Kretzler, M., Leiter, E.H., 2009. Mouse models of diabetic nephropathy. J. Am. Soc. Nephrol. 20 (12), 2503–2512.
CDC. National Diabetes Statistics Report 2022 [cited 2022 March 15 2022]. Available from: https://www.cdc.gov/diabetes/data/statistics-report/index.html.
Damasiewicz MJ, Nickolas TL. Rethinking Bone Disease in Kidney Disease. JBMR plus. 2018;2(6):309–22. Epub 20181115. doi: https://doi.org/10.1002/jbm4.10117. PubMed PMID: 30460334; PMCID: PMC6237213.
Damrath, J.G., Creecy, A., Wallace, J.M., Moe, S.M., 2021. The impact of advanced glycation end products on bone properties in chronic kidney disease. Curr. Opin. Nephrol. Hypertens. 30 (4), 411–417.
Damrath, J.G., Metzger, C., Allen, M., Wallace, J.M., 2022. A novel murine model of combined type 1 diabetes and chronic kidney disease has greater skeletal detriments than either disease individually. Bone 165, 116559.
Deeds, M.C., Anderson, J.M., Armstrong, A.S., Gastineau, D.A., Hiddinga, H.J., Jahangir, A., Eberhardt, N.L., Kudva, Y.C., 2011. Single dose streptozotocin-induced diabetes: considerations for study design in islet transplantation models. Lab. Anim. 45 (3), 131–140. https://doi.org/10.1258/la.2010.010090 (PubMed PMID: 21478271).
Eckert, A.J., Semler, O., Schnabel, D., Köstner, K., Wurm, D., Bechtold-Dalla Pozza, S., Schaaf, K., Hörtenhuber, T., Hammersen, J., Holl, R.W., 2021. Bone fractures in children and young adults with type 1 diabetes: age distribution, fracture location, and the role of glycemic control. J. Bone Miner. Res. Off. J. Am. Soc. Bone Miner. Res. 36 (12), 2371–2380.
Farr, J.N., Khosla, S., 2016. Determinants of bone strength and quality in diabetes mellitus in humans. Bone 82, 28–34.
Furman BL. Streptozotocin-induced diabetic models in mice and rats. Current protocols in pharmacology. 2015;70(1):5.47. 1–5.. 20.
Geusens, P., Appelman-Dijkstra, N., Lems, W., van den Bergh, J., 2023. Romosozumab for the treatment of postmenopausal women at high risk of fracture. Expert. Opin. Biol. Ther. 23 (1), 11–19.
Goyal, S.N., Reddy, N.M., Patil, K.R., Nakhate, K.T., Ojha, S., Patil, C.R., Agrawal, Y.O., 2016. Challenges and issues with streptozotocin-induced diabetes – a clinically relevant animal model to understand the diabetes pathogenesis and evaluate therapeutics. Chem. Biol. Interact. 244, 49–63. https://doi.org/10.1016/j.cbi.2015.11.032.
Gurley SB, Clare SE, Snow KP, Hu A, Meyer TW, Coffman TM. Impact of genetic background on nephropathy in diabetic mice. Am. J. Physiol. Ren. Physiol. 2006;290 (1):F214–22. Epub 20050823. doi: https://doi.org/10.1152/ajprenal.00204.2005. PubMed PMID: 16118394.
Ha J, Jeong C, Han KD, Lim Y, Kim MK, Kwon HS, Song KH, Kang MI, Baek KH. Comparison of fracture risk between type 1 and type 2 diabetes: a comprehensive real-world data. Osteoporosis international : a journal established as result of cooperation between the European Foundation for Osteoporosis and the National Osteoporosis Foundation of the USA. 2021;32(12):2543–53. Epub 20210731. doi: https://doi.org/10.1007/s00198-021-06032-z. PubMed PMID: 34333678.
Hasegawa, T., Tokunaga, S., Yamamoto, T., Sakai, M., Hongo, H., Kawata, T., Amizuka, N., 2023. Evocalcet rescues secondary hyperparathyroidism-driven cortical porosity in CKD male rats. Endocrinology 164 (4). https://doi.org/10.1210/endocr/bqad022 (PubMed PMID: 36718587; PMCID: PMC9939342).

Hatch, J.M., Segvich, D.M., Kohler, R., Wallace, J.M., 2022. Skeletal manifestations in a streptozotocin-induced C57BL/6 model of type 1 diabetes. Bone Rep. 17, 101609.
Hsu, C.P., Maddox, J., Block, G., Bartley, Y., Yu, Z., 2022. Influence of renal function on pharmacokinetics, pharmacodynamics, and safety of a single dose of Romosozumab. J. Clin. Pharmacol. 62 (9), 1132–1141.
Jacobson A, Tastad CA, Creecy A, Wallace JM. Combined thermoneutral housing and raloxifene treatment improves trabecular bone microarchitecture and strength in growing female mice. Calcif. Tissue Int. 2023;112(3):359–62. Epub 20221113. doi: https://doi.org/10.1007/s00223-022-01038-z. PubMed PMID: 36371724.
Jelinek, H.F., Osman, W.M., Khandoker, A.H., Khalaf, K., Lee, S., Almahmeed, W., Alsafar, H.S., 2017. Clinical profiles, comorbidities and complications of type 2 diabetes mellitus in patients from United Arab Emirates. BMJ Open Diabetes Res. Care 5 (1), e000427.
Karim, L., Vashishth, D., 2012. Heterogeneous glycation of cancellous bone and its association with bone quality and fragility. PLoS One 7(4):e35047. Epub 20120413. https://doi.org/10.1371/journal.pone.0035047 (PubMed PMID: 22514706; PMCID: PMC3325937).
King, A.J., 2012. The use of animal models in diabetes research. Br. J. Pharmacol. 166 (3), 877–894.
Kohler, R., Tastad, C.A., Stacy, A.J., Swallow, E.A., Metzger, C.E., Allen, M.R., Wallace, J. M., 2021. The effect of single versus group μCT on the detection of trabecular and cortical disease phenotypes in mouse bones. JBMR Plus. https://doi.org/10.1002/jbm4.10473.
Leslie, W.D., Rubin, M.R., Schwartz, A.V., Kanis, J.A., 2012. Type 2 diabetes and bone. J. Bone Miner. Res. 27 (11), 2231–2237.
Li, X., Ominsky, M.S., Warmington, K.S., Morony, S., Gong, J., Cao, J., Gao, Y., Shalhoub, V., Tipton, B., Haldankar, R., Chen, Q., Winters, A., Boone, T., Geng, Z., Niu, Q.T., Ke, H.Z., Kostenuik, P.J., Simonet, W.S., Lacey, D.L., Paszty, C., 2009. Sclerostin antibody treatment increases bone formation, bone mass, and bone strength in a rat model of postmenopausal osteoporosis. J. Bone Miner. Res. 24 (4), 578–588. https://doi.org/10.1359/jbmr.081206 (PubMed PMID: 19049336).
Limaye A, editor. Drishti: a volume exploration and presentation tool. Developments in X-ray Tomography VIII; 2012: Int. Soc. Opt. Phot.
Marino, S., Akel, N., Li, S., Cregor, M., Jones, M., Perez, B., Troncoso, G., Meeks, J., Stewart, S., Sato, A.Y., Nookaew, I., Bellido, T., 2023. Reversal of the diabetic bone signature with anabolic therapies in mice. Bone Res. 11(1):19. Epub 20230419 https://doi.org/10.1038/s41413-023-00261-0 (PubMed PMID: 37076478; PMCID: PMC10115794).
McClung MR, Grauer A, Boonen S, Bolognese MA, Brown JP, Diez-Perez A, Langdahl BL, Reginster JY, Zanchetta JR, Wasserman SM, Katz L, Maddox J, Yang YC, Libanati C, Bone HG. Romosozumab in postmenopausal women with low bone mineral density. N. Engl. J. Med. 2014;370(5):412–20. Epub 20140101. doi: https://doi.org/10.1056/NEJMoa1305224. PubMed PMID: 24382002.
Metzger CE, Swallow EA, Allen MR. Elevations in cortical porosity occur prior to significant rise in serum parathyroid hormone in young female mice with adenine-induced CKD. Calcif. Tissue Int. 2020;106(4):392–400. Epub 2019/12/14. doi: https://doi.org/10.1007/s00223-019-00642-w. PubMed PMID: 31832725.
Metzger, C.E., Swallow, E.A., Stacy, A.J., Allen, M.R., 2021. Adenine-induced chronic kidney disease induces a similar skeletal phenotype in male and female C57BL/6 mice with more severe deficits in cortical bone properties of male mice. PLoS One 16 (4), e0250438.
Miller, P.D., Adachi, J.D., Albergaria, B.H., Cheung, A.M., Chines, A.A., Gielen, E., Langdahl, B.L., Miyauchi, A., Oates, M., Reid, I.R., 2022. Efficacy and safety of romosozumab among postmenopausal women with osteoporosis and mild-to-moderate chronic kidney disease. J. Bone Miner. Res. 37 (8), 1437–1445.
Misof, B.M., Blouin, S., Roschger, P., Werzowa, J., Klaushofer, K., Lehmann, G., 2019. Bone matrix mineralization and osteocyte lacunae characteristics in patients with chronic kidney disease - mineral bone disorder (CKD-MBD). J. Musculoskelet. Neuronal Intereact. 19 (2), 196–206.
Miyauchi, A., Hamaya, E., Nishi, K., Tolman, C., Shimauchi, J., 2022. Efficacy and safety of romosozumab among Japanese postmenopausal women with osteoporosis and mild-to-moderate chronic kidney disease. J. Bone Miner. Metab. 1-11.
Moseley, K.F., 2012. Type 2 diabetes and bone fractures. Curr. Opin. Endocrinol. Diabetes Obes. 19 (2), 128.
Navaneethan, S.D., Zoungas, S., Caramori, M.L., Chan, J.C.N., Heerspink, H.J.L., Hurst, C., Liew, A., Michos, E.D., Olowu, W.A., Sadusky, T., Tandon, N., Tuttle, K.R., Wanner, C., Wilkens, K.G., Lytvyn, L., Craig, J.C., Tunnicliffe, D.J., Howell, M., Tonelli, M., Cheung, M., Earley, A., Rossing, P., de Boer, I.H., Khunti, K., 2021. Diabetes management in chronic kidney disease: synopsis of the 2020 KDIGO clinical practice guideline. Ann. Intern. Med. 174 (3), 385–394. Epub 2020/11/10. https://doi.org/10.7326/M20-5938. 33166222.
Ominsky, M.S., Boyce, R.W., Li, X., Ke, H.Z., 2017. Effects of sclerostin antibodies in animal models of osteoporosis. Bone 96, 63–75. https://doi.org/10.1016/j.bone.2016.10.019.
Qi, Z., Fujita, H., Jin, J., Davis, L.S., Wang, Y., Fogo, A.B., Breyer, M.D., 2005. Characterization of susceptibility of inbred mouse strains to diabetic nephropathy. Diabetes 54 (9), 2628–2637. https://doi.org/10.2337/diabetes.54.9.2628.
Reul, O.N., Anneken, A.M., Kohler, R.K., Segvich, D.M., Wallace, J.M., 2023. Practical considerations for the design, execution, and interpretation of studies involving whole-Bone bending tests of rodent bones. J. Visualized Exp. 199.
Reyes-García, R., Rozas-Moreno, P., López-Gallardo, G., García-Martín, A., Varsavsky, M., Avilés-Perez, M.D., Muñoz-Torres, M., 2013. Serum levels of bone resorption markers are decreased in patients with type 2 diabetes. Acta Diabetol. 50 (1), 47–52.
Rubin, M.R., Dempster, D.W., Sliney Jr., J., Zhou, H., Nickolas, T.L., Stein, E.M., Dworakowski, E., Dellabadia, M., Ives, R., McMahon, D.J., 2011. PTH (1–84) administration reverses abnormal bone-remodeling dynamics and structure in hypoparathyroidism. J. Bone Miner. Res. 26 (11), 2727–2736.
Saag KG, Petersen J, Brandi ML, Karaplis AC, Lorentzon M, Thomas T, Maddox J, Fan M, Meisner PD, Grauer A. Romosozumab or alendronate for fracture prevention in women with osteoporosis. N. Engl. J. Med. 2017;377(15):1417–27. Epub 20170911. doi: https://doi.org/10.1056/NEJMoa1708322. PubMed PMID: 28892457.
Saito, T., Mizobuchi, M., Kato, T., Suzuki, T., Fujiwara, Y., Kanamori, N., Makuuchi, M., Honda, H., 2023. One-year romosozumab treatment followed by one-year denosumab treatment for osteoporosis in patients on hemodialysis: an observational study. Calcif. Tissue Int. 112 (1), 34–44.
Sato M, Inaba M, Yamada S, Emoto M, Ohno Y, Tsujimoto Y. Efficacy of romosozumab in patients with osteoporosis on maintenance hemodialysis in Japan; an observational study. J. Bone Miner. Metab. 2021;39(6):1082–90. Epub 20210729. doi: https://doi.org/10.1007/s00774-021-01253-y. PubMed PMID: 34324082.
Sharma, K., Jin, Y., Guo, J., Ziyadeh, F.N., 1996. Neutralization of TGF-β by anti-TGF-β antibody attenuates kidney hypertrophy and the enhanced extracellular matrix gene expression in STZ-induced diabetic mice. Diabetes 45, 522–530.
Sikjaer, T., Rejnmark, L., Thomsen, J.S., Tietze, A., Brüel, A., Andersen, G., Mosekilde, L., 2012. Changes in 3-dimensional bone structure indices in hypoparathyroid patients treated with PTH (1-84): a randomized controlled study. J. Bone Miner. Res. 27 (4), 781–788.
Sinder, B.P., Lloyd, W.R., Salemi, J.D., Marini, J.C., Caird, M.S., Morris, M.D., Kozloff, K. M., 2016. Effect of anti-sclerostin therapy and osteogenesis imperfecta on tissue-level properties in growing and adult mice while controlling for tissue age. Bone 84, 222–229.
Suzuki, T., Mizobuchi, M., Yoshida, S., Terado, N., Aoki, S., Sato, N., Honda, H., 2022. Romosozumab successfully regulated progressive osteoporosis in a patient with autosomal dominant polycystic kidney disease undergoing hemodialysis. Osteoporos. Int. 1-4.
Vashishth D, Gibson GJ, Khoury JI, Schaffler MB, Kimura J, Fyhrie DP. Influence of nonenzymatic glycation on biomechanical properties of cortical bone. Bone 2001;28 (2):195–201. doi: https://doi.org/https://doi.org/10.1016/S8756-3282(00)00434-8.
Vestergaard P. Discrepancies in bone mineral density and fracture risk in patients with type 1 and type 2 diabetes–a meta-analysis. Osteoporosis international : a journal established as result of cooperation between the European Foundation for Osteoporosis and the National Osteoporosis Foundation of the USA. 2007;18(4):427–44. Epub 20061027. doi: https://doi.org/10.1007/s00198-006-0253-4. PubMed PMID: 17068657.
Virtue, S., Vidal-Puig, A., 2021. GTTs and ITTs in mice: simple tests, complex answers. Nat. Metab. 3, 883–886.
Weber, D.R., Haynes, K., Leonard, M.B., Willi, S.M., Denburg, M.R., 2015. Type 1 diabetes is associated with an increased risk of fracture across the life span: a population-based cohort study using The Health Improvement Network (THIN). Diabetes Care 38 (10), 1913–1920.